## **OPEN ACCESS**



## GRB 200829A: External-shock Origin of the Very Early Prompt Emission?

Jing Li<sup>1</sup>, Da-Bin Lin<sup>1</sup>, Rui-Jing Lu<sup>1</sup>, Lu-Yao Jiang<sup>2,3</sup>, Wen-Qiang Liang<sup>1</sup>, Zhi-Lin Chen<sup>1</sup>, Xiao-Yan Li<sup>1</sup>, Xiang-Gao Wang<sup>1</sup>, and En-Wei Liang<sup>1</sup>

## Abstract

Long-duration GRB 200829A was detected by Fermi-GBM and Swift-BAT/XRT, and then rapidly observed by other ground-based telescopes. It has a weak  $\gamma$ -ray emission in the very early phase and is followed by a bright spiky  $\gamma$ -ray emission pulse. The radiation spectrum of the very early emission is best fitted by a power-law function with index  $\sim$ -1.7. However, the bright spiky  $\gamma$ -ray pulse, especially the time around the peak, exhibits a distinct two-component radiation spectrum, i.e., Band function combined with a blackbody radiation spectrum. We infer the photospheric properties and reveal a medium magnetization at a photospheric position by adopting the initial size of the outflow as  $r_0=10^9$  cm. It implies that the Band component in this pulse may be formed during the dissipation of the magnetic field. The power-law radiation spectra found in the very early prompt emission may imply the external-shock origination of this phase. Then, we perform the Markov Chain Monte Carlo method fitting on the light curves of this burst, where the jet corresponding to the  $\gamma$ -ray pulse at around 20 s is used to refresh the external shock. It is shown that the light curves of the very early phase and X-ray afterglow after 40 s, involving the X-ray bump at around 100 s, can be well modeled in the external-shock scenario. For the obtained initial outflow, we estimate the minimum magnetization factor of the jet based on the fact that the photospheric emission of this jet is missed in the very early phase.

Unified Astronomy Thesaurus concepts: Gamma-ray bursts (629)

### 1. Introduction

Theoretically, it is generally believed that gamma-ray bursts (GRBs) originated from the collapse of massive stars or mergers of double compact stars (e.g., Colgate 1974; Paczynski 1986; Eichler et al. 1989; Narayan et al. 1992; Woosley 1993; MacFadyen & Woosley 1999; Piran 2004; Zhang & Mészáros 2004; Woosley & Bloom 2006; Kumar & Zhang 2015). Observationally, GRBs generally appear as brief and intense  $\gamma$ -rays followed by a long-lived afterglow emission. The prompt  $\gamma$ -rays are highly variable with a duration from millisecond to thousands of seconds. The observational spectra are usually well fitted by an empirical function, characterized by a smoothly joint broken power-law (PL) function, the socalled Band function (Band et al. 1993) or a quasi-thermal spectral component that appears in the spectra of some GRBs. The previous observations demonstrated that thermal components exhibit different observational properties. They either can be detected during the entire duration of the prompt emission (e.g., Ghirlanda et al. 2013) or may be only found at the beginning of the burst duration, and subsequently appear with a nonthermal component. The detection of a diversified spectral characteristic shows that GRB ejecta may have a diverse jet composition. It may be neither fully matter-dominated ejecta nor fully magnetized outflows. More realistically, GRB outflows are likely to be a hybrid jet, which carries the two components simultaneously and launches at the central engine (e.g., Gao & Zhang 2015). The light curves of afterglow

Original content from this work may be used under the terms of the Creative Commons Attribution 4.0 licence. Any further distribution of this work must maintain attribution to the author(s) and the title of the work, journal citation and DOI.

emission usually can be decomposed into four PL segments, i.e., an initial steep decay, a shallow decay, a normal decay, and a late steeper decay, sometimes accompanied by one or several flares (Nousek et al. 2006; Zhang et al. 2006). It is commonly believed that the multiwavelength afterglow is mainly from the external shock, which is formed during a relativistic jet propagating in the circum-burst medium (e.g., Mészáros & Rees 1997). However, the origin of the prompt  $\gamma$ -rays is not well understood. The prompt  $\gamma$ -rays may be from the internal shock in an erratic relativistic fireball, a dissipative photosphere, a Poynting-flux dominated jet, or even an external shock (e.g., Rees & Meszaros 1992; Meszaros & Rees 1993; Rees & Meszaros 1994; Giannios 2008; Beloborodov 2010; Vurm et al. 2011; Zhang & Yan 2011; Burgess et al. 2016; Huang et al. 2018).

It is not a new idea that the prompt  $\gamma$ -rays of GRBs originate from the external shock. Burgess et al. (2016) have shown that the prompt emission of GRB 141028A very likely originated from an external shock. Huang et al. (2018) suggested that GRB 120729A is an external-shock origin for both the prompt  $\gamma$ -ray emission and afterglow. They also systematically investigate single pulse GRBs in the Swift's GRBs and find that a small fraction of GRBs (GRB 120729A, GRB 051111, and GRB 070318) are likely to originate from an external shock for both the prompt  $\gamma$ -ray emission and afterglow. However, Huang et al. (2018) focus on the bursts appearing as a single pulse from the prompt emission to its afterglow. In fact, the central engine of GRBs may reactivate and launch relativistic ejecta several times. The late-launched ejecta may be observed as flares in the afterglow and interact with the external shock at a later period. The burst GRB 200829A may be in the above scenarios. GRB 200829A was detected by Fermi-GBM and

<sup>&</sup>lt;sup>1</sup> Guangxi Key Laboratory for Relativistic Astrophysics, School of Physical Science and Technology, Guangxi University, Nanning 530004, People's Republic of China; lindabin@gxu.edu.cn, luruijing@gxu.edu.cn

<sup>&</sup>lt;sup>2</sup> Key Laboratory of Dark Matter and Space Astronomy, Purple Mountain Observatory, Chinese Academy of Sciences, Nanjing 210034, People's Republic of China School of Astronomy and Space Science, University of Science and Technology of China, Hefei, Anhui 230026, People's Republic of China Received 2022 February 25; revised 2022 December 23; accepted 2023 January 1; published 2023 February 9

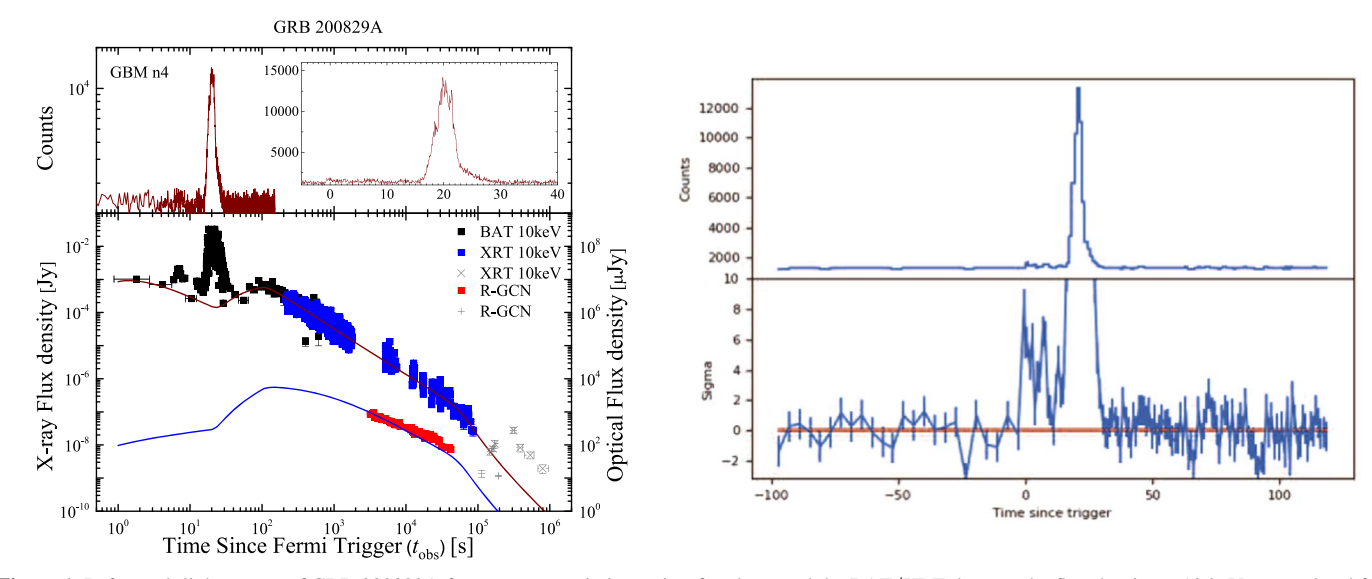


Figure 1. Left panel: light curves of GRB 200829A from prompt emission to its afterglows and the BAT/XRT data are the flux density at 10 keV extrapolated from BAT/XRT observation, where the inset of the upper-right panel shows the prompt  $\gamma$ -rays in the linear spaces. The Markov Chain Monte Carlo fitting result based on the model in Appendix B is shown with a dark-red line and blue line for X-ray and optical data, respectively. Here, the data showed with gray "×" and "+" symbols are not used in our fittings. Right panel: GBM light curve of GRB 200829A without background subtracted (upper panel) and the signal significance (bottom panel), where the background was estimated by fitting the light curve before and after the burst with a polynomial model. It reveals that there is a significant amount of photons in the period of [0, 10] s from GRB 200829A.

Swift-BAT/XRT, and the light curve of prompt emission is composed of an initial very early weak emission (with a duration  $\sim 5$  s) followed by a bright spiky  $\gamma$ -ray pulse with a duration  $\sim 10$  s. We find that the spectrum in the  $\gamma$ -ray pulse of GRB 200829A exhibits a distinct two-component, i.e., Band function combined with a blackbody radiation spectrum, especially in the peak time. It means that the thermal component should indeed exist, and GRB 200829A outflows are likely to be a hybrid jet. What's more, the radiation spectrum in its very early phase can be fitted with a PL spectral model with index  $\sim -1.7$ , which may be an indication of the origin of an external-forward shock. The central engine of GRB 200829A may reactivate and launch jets at different times, resulting in bright spiky  $\gamma$ -ray pulses when jets collide with each other.

This paper presents a detailed analysis of  $\gamma$ -rays and X-ray emission from the long GRB 200829A detected by Fermi and Swift. The paper is organized as follows. In Section 2, we introduce the observations and light-curve features of GRB 200829A. In Section 3, the detailed analysis and results of GRB 200829A are performed, and we also analyze the other properties of GRB 200829A in a different phase. In Section 4, the summary and discussions are presented.

## 2. Observations and Data Reduction

The long GRB 200829A was first detected by Fermi Gamma-Ray Burst Monitor (GBM) at 13: 58: 14.66 UT ( $T_0$ ) on 2020 August 29 with duration  $T_{90} \sim 6.9 \, \mathrm{s}$  (Lesage et al. 2020). In addition to the Fermi-GBM, Swift-BAT triggered the burst at 13: 59: 34 UT on 2020 August 29 (Palmer et al. 2020), and Swift-XRT began to observe the burst at 128.7 s after the BAT trigger (Gropp et al. 2020). Oates et al. (2020) created a SED at 900 s after the BAT trigger and found a photometric redshift of  $z=1.25\pm0.02$  for this burst. The optical afterglow is detected in the first 2 days after the GRB trigger (Pozanenko et al. 2020b). In the left panels of Figure 1, we show the light curves of prompt  $\gamma$ -rays and afterglows of GRB 200829A with

respect to the Fermi trigger. The inset in the upper part of this panel shows the light curves of prompt emission based on the Fermi observation in the linear spaces. Here, the Fermi data are from the Fermi Science Support Center<sup>4</sup> and a GBM light curve and source spectra are extracted from the TTE (Time-Tagged-Events) data by using a python source package named *gtBurst*,<sup>5</sup> the BAT/XRT data are taken from the UK Swift Science Data Center,<sup>6</sup> and the optical data of GRB 200829A are from Siegel et al. (2020), Pozanenko et al. (2020a), Lipunov et al. (2020b), Kuin et al. (2020), Lipunov et al. (2020b), Thu et al. (2020b), Moskvitin et al. (2020a), Pankov et al. (2020), Zhu et al. (2020a), Izzo (2020), Volnova et al. (2020), De Pasquale (2020), Pozanenko et al. (2020b).

Based on the light curves in the left panels of Figure 1, one can find that the prompt  $\gamma$ -rays are dominated by bright spiky  $\gamma$ -ray pulses in the period of  $t_{\rm obs} \sim [15, 30]$  s based on GBM observation, which is preceded by a small  $\gamma$ -ray pulse in the period of  $t_{\rm obs} \sim [6, 10]$  s based on BAT observation. However, it should be noted that the small  $\gamma$ -ray pulse in the period of  $t_{\rm obs} \sim [6, 10]$  s is not significant in the light curve of GBM observation. Except for these two  $\gamma$ -ray episodes, there is a significant  $\gamma$ -ray emission in the very early phase of the prompt emission ( $t_{\rm obs}$  < 6 s) based on BAT observation. This can also be found in the right panels of Figure 1, which shows the GBM light curve of GRB 200829A without background subtracted (upper panel) and the signal significance (bottom panel). One can find that the signal significance in the period of  $\sim$ [0, 10] s is higher than  $\sim 4\sigma$ , which reveals significant  $\gamma$ -ray photons in this period. In Section 3, we present detailed studies on the spectra and the corresponding physical implications for the very early phase and the bright spiky  $\gamma$ -ray pulses.

https://fermi.gsfc.nasa.gov/ssc/data/access/

https://github.com/giacomov/gtburst

<sup>6</sup> http://www.swift.ac.uk/burst\_analyser/00993768/

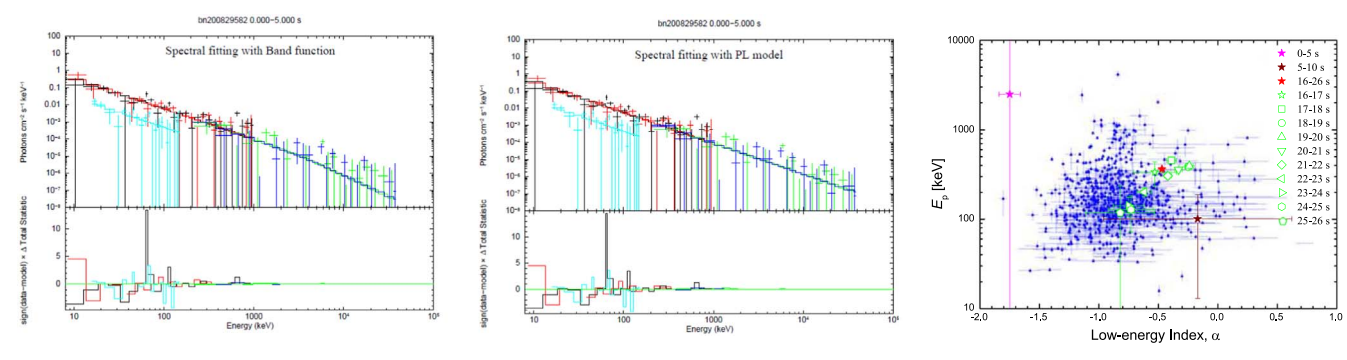


Figure 2. Spectral fitting results of the very early prompt emission ( $t_{obs} \in [0, 5]$  s) in GRB 200829A. Here, the joint spectral fitting by combining Swift-BAT and Fermi-GBM observations based on the Band function (left panel) or PL function (middle panel) is performed. In addition, the relation of  $E_p$  and  $\alpha$  based on the spectral fitting results with the Band function are plotted in the right panel with " $\star$ " symbols, where the blue symbols are from Poolakkil et al. (2021). Here, the different green hollow symbols are the time-resolved spectral fitting results in the period of [16, 26] s.

 Table 1

 Spectral Fitting Results of the Very Early Prompt Emission in GRB 200829A

| Time Interval (s) | Model        | $\alpha \text{ (or } \hat{\Gamma})^{a}$ | β                                    | $E_0(\text{keV})$                   | $N_0^{b}$                             | $\chi_r^2$   |
|-------------------|--------------|---|--------------------------------------|-------------------------------------|---------------------------------------|--------------|
| [0, 5]            | PL           | $-1.79 \pm 0.06$                        | •••                                  | •••                                 | $21.59 \pm 5.98$                      | 1.08         |
| [0, 5]<br>[5, 10] | Band<br>Band | $-1.75 \pm 0.09 \\ -0.17 \pm 0.79$      | $-2.42 \pm 5.08$<br>$-2.25 \pm 0.27$ | 9976.67 ± 51113.36<br>54.94 ± 41.55 | $0.006 \pm 0.0006$<br>$0.05 \pm 0.06$ | 1.08<br>0.99 |

#### Notes.

<sup>b</sup>  $N_0$  is in unit of photons  $\cdot$  cm<sup>-2</sup>  $\cdot$  s<sup>-1</sup>  $\cdot$  keV<sup>-1</sup>.

## 3. Detailed Analysis of GRB 200829A and Results

## 3.1. Very Early Prompt $\gamma$ -Ray Emission

For the very early phase of the prompt emission, the spectral fitting with the Band function reports the values of  $\alpha =$  $-1.75 \pm 0.09$ ,  $E_0 = 9976.67 \pm 51113.36$ , and  $\beta = -2.42 \pm 0.09$ 5.08 (see the third line of Table 1). The values of  $E_0$  and  $\beta$ could not be well constrained from the spectral fitting. Then, we perform the spectral analysis of the very early phase with the PL function<sup>8</sup> or cutoff PL (CPL) function. Here, the spectral fitting with the PL function reports the PL index  $\ddot{\Gamma} = -1.79 \pm 0.06$  (see the second line of Table 1), the spectral fitting with the CPL function could not present a good fitting, and the corresponding result is not reported. The spectral fitting results for the very early prompt emission with the Band function (left panel) and PL function (middle panel) are also shown in Figure 2. We note that the values of  $\alpha = -1.75 \pm 0.09$  and  $\hat{\Gamma} = -1.75 \pm 0.06$  from the spectral fittings are almost the same. Here, the value of  $\alpha$  can be well constrained in the spectral fitting with the Band function. This fact may imply that the intrinsic radiation spectrum in this period may be consistent with a PL spectral model with  $\hat{\Gamma} \sim -1.7$  or a Band function with a break at  $\sim 10$  MeV and PL index  $\sim$ -1.7 in its low-energy regime ( $E \lesssim 10 \text{ MeV}$ ).

The reasons are as follows. First, the spectral fitting on such kind of intrinsic radiation spectrum with a Band function would

not provide a good constraint on the value of  $E_0$  and thus  $\beta$ . This is consistent with our spectral fitting result for this period based on a Band function. In addition, a Band function with a break at  $\sim 10$  MeV, the PL index  $\sim -1.7$  in its low-energy regime ( $E \lesssim 10$  MeV), and the PL index  $\gtrsim -2.5$  in its high-energy regime ( $E \gtrsim 10$  MeV) can be modeled with a PL function and  $\hat{\Gamma} = -1.79$  in Fermi-GBM energy band (8 keV–40 MeV). This is also consistent with our spectral fitting result for this period based on a PL function. Second and importantly, we perform the spectral fitting on the Swift-BAT observation for this period based on a PL model, and the value of  $\hat{\Gamma} = -1.71$  is reported.

We note that such kind of intrinsic radiation spectrum is very different from the general Band radiation component of GRBs' prompt emission, of which the value of  $\alpha$  is around -1 and the break energy  $E_0$  is around 400 keV. The right panel of Figure 2 shows the relation of  $E_{\rm p}$  and  $\alpha$  based on the spectral fitting results with a Band function, where the blue symbols are from Figure 8 of Poolakkil et al. (2021) and represent the GOOD sample for time-integrated spectral fits with Band function. In this panel, the spectral analysis result for the very early phase of the prompt emission based on the Band function is also tentatively shown with pink " $\star$ " even though the value of  $E_0$ could not be well constrained, and the spectral fitting results of the small  $\gamma$ -ray pulse ([5, 10] s) or the bright spiky  $\gamma$ -ray pulses ([16, 26] s) with Band function are also shown. One can find that such a radiation spectrum is very different from the general Band radiation component of GRBs' prompt emission, involving that of the bright spiky  $\gamma$ -ray pulses or the small  $\gamma$ ray pulse. Then, we would like to believe that the very early phase of the prompt emission in this burst may be originated from the other channel rather than that for the bright spiky  $\gamma$ ray pulses or the small  $\gamma$ -ray pulse.

<sup>&</sup>lt;sup>a</sup> The photon spectral index  $\hat{\Gamma}$  is for the PL model and  $\alpha$  is for the Band function model.

Band function is described as  $N(E) = N_0(E/100\text{keV})^{\alpha} \exp(-E/E_0)$  for  $E \le (\alpha - \beta)E_0$  and  $N(E) = N_0[(\alpha - \beta)E_0/100\text{keV}]^{\alpha-\beta} \exp(\beta - \alpha)(E/100\text{keV})^{\beta}$  for  $E \ge (\alpha - \beta)E_0$ , where  $N_0$  is the normalization, and  $\alpha$ ,  $\beta$ , and  $E_0$  are parameters in the spectral fittings. The peak photon energy of  $E^2N(E)$  is  $E_p = (\alpha + 2)E_0$ .

<sup>&</sup>lt;sup>8</sup> The PL function is described as  $N(E) = N_0 (E/1 \text{keV})^{\hat{\Gamma}}$  with  $\hat{\Gamma}$  being the photon spectral index.

<sup>&</sup>lt;sup>9</sup> Please see Appendix A for a comprehensive analysis of the radiation spectrum in this period.

## 3.2. Bright Spiky \(\gamma\)-Ray Pulse and Deriving Physical Parameters

There is a bright spiky  $\gamma$ -ray pulse appearing at  $t_{\rm obs} \sim [16,$ 26] s after the Fermi trigger. In order to perform a detailed analysis of this pulse, we divide this pulse into several time intervals with 1 s time span and perform the spectral fitting on these time intervals with the Band function. The spectral fitting results are reported in Table 2 and shown in the left panels of Figure 3. A distinct multicomponent of radiation spectrum is found in several time intervals of this pulse, e.g., [18, 19] s. Then, we also perform the spectral analysis together with the Band function and a blackbody radiation component (BB), <sup>10</sup> i.e., "Band+BB." The spectral fitting results based on the Band +BB model are also reported in Table 2 and shown in the right panels of Figure 3. We also estimate the Bayesian Information Criterion (BIC; Schwarz 1978) for the spectral fitting with the Band function and that with the Band+BB model. The values of BIC from the spectral analysis are also reported in Table 2. The BIC is adopted to evaluate the goodness of the model fitting, taking into account the model complexity and the different numbers of free parameters. Generally, the model with the lowest BIC is preferred. By comparing the values of BIC from the spectral analysis, one can find that the Band+BB model is preferred for the radiation spectrum of the time intervals around the peak of the bright spiky  $\gamma$ -ray pulse. Since the value of  $\Delta BIC = BIC_{Band} - BIC_{Band+BB}$  is in the range of 12–25, it is strong to support a blackbody component in these time intervals. 11

The temperature and flux of the blackbody component, together with the radius of the jet base (size of the central engine)  $r_0$  and z, can provide useful information about the physics of the photosphere. Meanwhile, due to the presence of the Band energy spectrum component, the jet compositions of GRB 200829A may be hybrid. Therefore, following Gao & Zhang (2015), we estimate the radius and Lorentz factor of the photosphere based on the blackbody component found in the period of [18,22] s by assuming the hybrid outflow of GRB 200829A. In the calculations, we assume that there is no dissipation below the photosphere and that the radiation efficiency  $\sim$ 52.1% (please see Section 4). The results are shown in the left panels of Figure 4; the blue and olive symbols are the physical quantities calculated based on  $r_0 = 10^8$  cm and  $r_0 = 10^9$  cm, and solid and hollow " $\star$ " represent the physical parameters  $r_{\rm ph}$ ,  $\Gamma_{\rm ph}$ , respectively. It indicates that the value of  $r_{\rm ph}$  increases with time and  $\Gamma_{\rm ph}$  remains constant at a low value of  $r_0$  and when  $r_0$  is large, it increases and eventually declines. We also infer the dimensionless entropy  $\eta$  and the magnetization factor  $\sigma$ , where  $\sigma_0$  and  $\sigma_{ph}$  are the magnetization factor of the outflow at  $r_0$  and  $r_{\rm ph}$ , respectively. The results are shown in the middle panels of Figure 4, the blue and olive symbols are the same as those in the left panels of Figure 4, and solid and hollow " $\star$ " represent the physical parameters  $\eta$ ,  $1 + \sigma_{ph}$ , and  $1+\sigma_0$ , respectively. It is shown that the dimensionless entropy  $\eta$  fluctuates in the range of 100–300. In addition, the values of  $1+\sigma_{\rm ph}$  can be around 5 if  $r_0=10^9$  cm is adopted and around 1 if  $r_0=10^8$  cm is adopted. Together with the Band and BB components found in this burst, the initial radius of the outflow producing the bright spiky  $\gamma$ -rays should be around or larger than  $10^9$  cm, i.e.,  $r_0 \gtrsim 10^9$  cm. This result is consistent with that found in GRBs with identified photospheric emission, e.g., GRB 120323A, GRB 131014A, and GRB 220426A (e.g., Guiriec et al. 2013, 2015; Deng et al. 2022). The nonthermal component in the bright spiky  $\gamma$ -rays, i.e., the Band component, seems to be formed during the dissipation of the magnetic energy.

## 3.3. Afterglow Analysis and a Self-consistent Paradigm for Bursting

Following the prompt  $\gamma$ -ray emission in this burst, a late bump appears at  $t_{\rm obs} > 40\,{\rm s}$  with a rising in the period of  $t_{\rm obs} \sim [40,\ 100]\,{\rm s}$  and a decaying after  $t_{\rm obs} \sim 100\,{\rm s}$ . It is reasonable to believe that the decaying phase of the late bump is the normal decay of the external-forward shock. For the X-ray emission in this phase, the closure relation (Zhang & Mészáros 2004) of  $\alpha \approx 3\beta/2$  with  $F \propto \nu^{-\beta} t^{-\alpha}$  can be found, where the value of  $\alpha = 1.30 \pm 0.03$  and  $\beta = 0.80 \pm 0.05$  are obtained based on the observations of Swift. It reveals that the X-ray emission in this phase is in the spectral regime of  $\nu_{\rm m} < \nu < \nu_{\rm c}$  for an external-forward shock in the interstellar medium.

The very early phase of the prompt emission may have originated from the external shock. The reasons are as follows. First, we have performed a joint spectral analysis by combining the observations of Swift-BAT and Fermi-GBM for the very early phase of the prompt emission in Section 3.1. The spectral analysis reveals that the very early phase of the prompt emission in this burst may be originated from the other channel rather than that for the small  $\gamma$ -ray pulse or the bright spiky  $\gamma$ ray pulses. Second, the radiation spectrum in this phase is strongly reminiscent of the GRB 120729A, of which the radiation spectrum in the prompt emission for the Fermi-GBM energy band can be well modeled with a PL function and photon spectral index  $\hat{\Gamma} \sim -1.47^{12}$  (Huang et al. 2018). Since the light curve of the prompt emission in GRB 120729A appears as a single long and smooth pulse, which extends continuously to the X-rays, it is suggested that both the prompt emission and the afterglows originated from an externalforward shock (Huang et al. 2018). Third, the spectral index of the very early prompt emission based on Swift-BAT and Fermi-GBM observations is almost the same as that of the decaying phase in the late bump based on the Swift-XRT observation (see Table 1 and Table 3). This is different from that in GRB 120729A, of which the spectral index in the X-ray energy band evolves from -1.47 in the early phase of the prompt emission to -1.83 in the late phase of afterglow. It may reveal that the X-rays may be the same spectral regime in GRB 200829A but in a different spectral regime in GRB 120729A for the very early prompt emission and the late phase of afterglow. Then, we would like to believe that the early phase of prompt emission ( $t_{obs} < 6$  s) has the same origination as that

 $<sup>\</sup>overline{^{10}}$   $N_{\rm BB}(E) = \frac{8.0525 \times KE^2}{(kT)^4(e^{(E/kT)}-1)}$ , where kT is the blackbody temperature keV; K is the  $L_{39}/D_{10}^2$ , where  $L_{39}$  is the source luminosity in units of  $10^{39}$  erg s<sup>-1</sup> and  $D_{10}$  is the distance to the source in units of 10 kpc.

In the spirit of Burnham & Anderson (2004), the value of  $\Delta BIC$  can be used as the strength of the evidence to allow a quick comparison and ranking of candidate hypotheses or models. For  $\Delta BIC = BIC_A - BIC_B$  with  $BIC_A > BIC_B$ , the strength of the evidence can be summarized as follows: the situation with  $\Delta BIC \leqslant 2$  provides no evidence against the model-A; the situation with  $\Delta BIC \leqslant 7$  provides positive evidence against the model-A; the situation with  $\Delta BIC \leqslant 7$  provides very strong evidence against the model-A (Burnham & Anderson 2004).

 $<sup>^{12}</sup>$  By performing joint spectral fitting of the Swift-BAT and Fermi-GBM observations for GRB 120729A, we obtain  $\hat{\Gamma} \sim -1.47$  and  $\hat{\Gamma} \sim -1.49$  for the period of [0, 10] s and [1, 2] s after the Fermi trigger, respectively.

5

Table 2 Spectral Fitting Results of the Bright Spicky  $\gamma$ -Ray Pulse in GRB 200829A

| Time Interval (s) |                  | Band               |                  |                 |        |                  |                     | Band + BB        |                    |                   |                   |        |                         |
|-------------------|------------------|--------------------|------------------|-----------------|--------|------------------|---------------------|------------------|--------------------|-------------------|-------------------|--------|-------------------------|
|                   | $\alpha$         | $E_0(\text{keV})$  | $\beta$          | $N_0^{\ a}$     | BIC    | $\alpha$         | $E_0(\text{keV})$   | $\beta$          | $N_0^{\mathrm{a}}$ | kT(keV)           | Ka                | BIC    | $\Delta \mathrm{BIC^b}$ |
| [16, 26]          | $-0.47 \pm 0.01$ | $231.41 \pm 4.11$  | $-2.47 \pm 0.02$ | $0.41 \pm 0.00$ | 948.83 | $-0.52 \pm 0.02$ | $286.22 \pm 9.53$   | $-2.56 \pm 0.02$ | $0.32 \pm 0.01$    | $32.82 \pm 1.68$  | $16.34 \pm 1.74$  | 841.76 | 107.07                  |
| [16, 17]          | $-0.53\pm0.18$   | $225.71 \pm 60.30$ | $-2.29\pm0.19$   | $0.06\pm0.01$   | 510.41 | $-0.80\pm0.20$   | $599.36 \pm 420.69$ | $-3.40\pm2.15$   | $0.02\pm0.00$      | $35.86\pm6.62$    | $7.19\pm1.95$     | 517.64 | -7.23                   |
| [17, 18]          | $-0.40\pm0.04$   | $283.01 \pm 16.61$ | $-2.83\pm0.13$   | $0.23\pm0.01$   | 550.50 | $-0.44\pm0.07$   | $350.38 \pm 34.98$  | $-3.15\pm0.24$   | $0.18\pm0.01$      | $42.30\pm5.88$    | $17.22\pm5.21$    | 548.53 | 1.96                    |
| [18, 19]          | $-0.25\pm0.03$   | $216.73 \pm 7.72$  | $-2.86\pm0.07$   | $0.58\pm0.01$   | 595.01 | $-0.31\pm0.05$   | $273.54 \pm 17.43$  | $-3.16\pm0.12$   | $0.41\pm0.02$      | $40.05 \pm 3.53$  | $39.41 \pm 7.56$  | 572.53 | 22.49                   |
| [19, 20]          | $-0.25\pm0.03$   | $221.12 \pm 7.34$  | $-2.32\pm0.02$   | $0.92\pm0.02$   | 536.65 | $-0.36\pm0.05$   | $297.34 \pm 26.24$  | $-2.38\pm0.03$   | $0.65\pm0.05$      | $42.56 \pm 3.85$  | $57.77 \pm 14.49$ | 523.84 | 12.81                   |
| [20, 21]          | $-0.32\pm0.03$   | $207.24 \pm 6.69$  | $-2.42\pm0.02$   | $1.04\pm0.02$   | 658.42 | $-0.40\pm0.05$   | $264.04 \pm 18.63$  | $-2.50\pm0.03$   | $0.76\pm0.05$      | $35.26 \pm 3.28$  | $47.93 \pm 10.16$ | 636.37 | 22.05                   |
| [21, 22]          | $-0.41 \pm 0.03$ | $188.50 \pm 7.07$  | $-2.59\pm0.04$   | $0.90\pm0.03$   | 601.88 | $-0.45\pm0.05$   | $232.22 \pm 15.55$  | $-2.71\pm0.06$   | $0.66\pm0.04$      | $27.89\pm2.56$    | $33.86\pm5.88$    | 576.20 | 25.67                   |
| [22, 23]          | $-0.60\pm0.06$   | $139.79 \pm 13.33$ | $-2.31\pm0.05$   | $0.41\pm0.03$   | 497.37 | $-0.84 \pm 0.11$ | $254.12 \pm 56.51$  | $-2.46\pm0.11$   | $0.22\pm0.04$      | $24.06 \pm 3.31$  | $13.07 \pm 4.12$  | 501.53 | -4.17                   |
| [23, 24]          | $-1.03 \pm 0.09$ | $195.52 \pm 37.43$ | $-2.45 \pm 0.17$ | $0.14\pm0.02$   | 490.10 | $-1.20\pm0.18$   | $340.63 \pm 181.20$ | $-2.48 \pm 0.31$ | $0.18\pm0.23$      | $23.79 \pm 3.84$  | $1.04 \pm 9.77$   | 495.21 | -5.11                   |
| [24, 25]          | $-0.59\pm0.23$   | $80.59 \pm 24.47$  | $-2.23\pm0.10$   | $0.22\pm0.08$   | 547.41 | $-1.35\pm0.15$   | $582.80 \pm 366.04$ | $-2.50\pm1.23$   | $0.04\pm0.01$      | $22.00 \pm 2.69$  | $7.76\pm1.46$     | 559.13 | -11.72                  |
| [25, 26]          | $-0.86\pm0.30$   | $102.82 \pm 56.82$ | $-2.19\pm0.16$   | $0.09\pm0.05$   | 513.84 | $-1.19\pm1.09$   | $203.83 \pm 657.78$ | $-2.13\pm0.24$   | $0.07\pm0.21$      | $21.75 \pm 10.54$ | $0.71\pm4.79$     | 526.66 | -12.82                  |

a  $N_0$  is in unit of photons  $\cdot$  cm<sup>-2</sup>  $\cdot$  s<sup>-1</sup>  $\cdot$  keV<sup>-1</sup>; K is the  $L_{39}/D_{10}^2$ , where  $L_{39}$  is the source luminosity in units of  $10^{39}$  erg s<sup>-1</sup> and  $D_{10}$  is the distance to the source in units of 10 kpc. b The  $\Delta$ BIC is the value of BIC<sub>Band</sub> – BIC<sub>Band+BB</sub>.

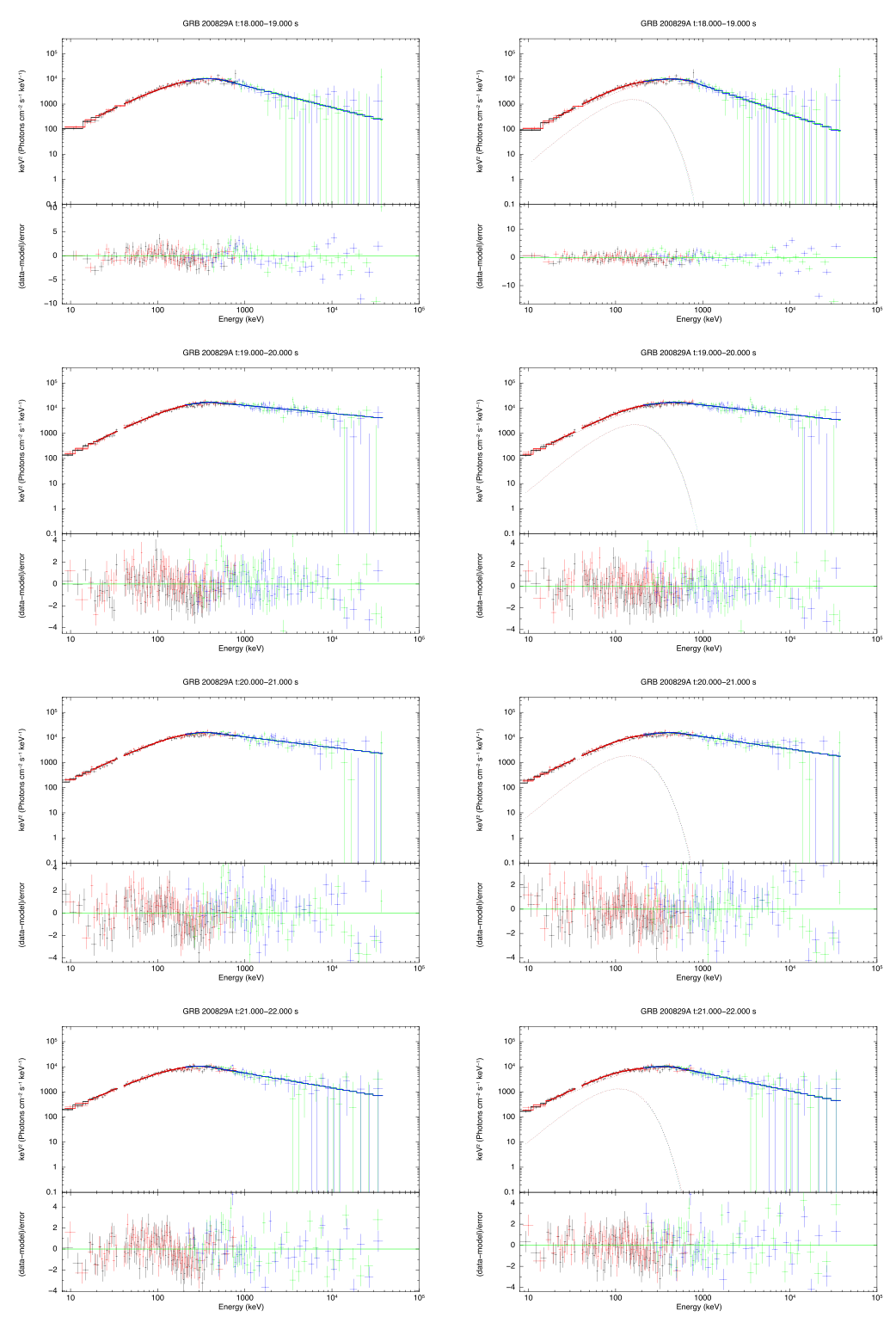


Figure 3. Spectral fitting results of the bright spiky  $\gamma$ -ray pulse in the period of  $t_{\text{obs}} \in [18, 22]$  s based on Band function (left panel) or Band+BB model (right panel).

of the decaying phase of the late bump, i.e., they all stem from the external-forward shock. In addition, the two  $\gamma$ -ray pulses in the period of  $\sim$ [6, 26] s should reflect the reactivity of the central engine of GRB 200829A.

Then, we suggest that the central engine of GRB 200829A may be intermittent and launch several episodes of ejecta separated by a long quiescent interval (Lin et al. 2018). The very early phase of the prompt emission originates from the

external shock, which is formed during the propagation of the first launched ejecta in the circum-burst medium. The later launched ejecta, of which the internal dissipation is responsible for the two  $\gamma$ -ray pulses, collide with the formed external shock in the period of  $t_{\rm obs} \sim [60, 100]$  s. Then, the energy injection into the external shock is presented in this period, and correspondingly a rising phase appears in the period of  $t_{\rm obs} \sim [60, 100]$  s. Based on the above paradigm, we fit the very early prompt

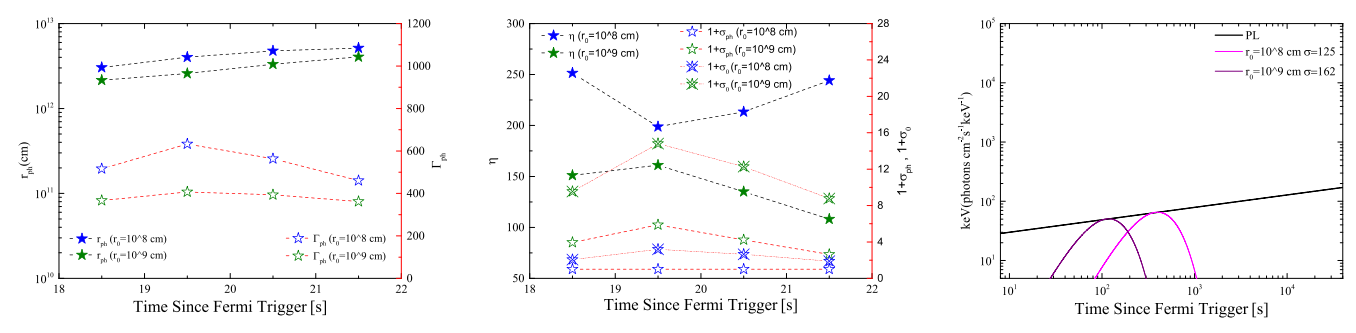


Figure 4. Left and middle panels: temporal evolution of derived properties  $(r_{\rm ph}, \Gamma_{\rm ph}, \eta, 1 + \sigma_{\rm ph}, \text{ and } 1 + \sigma_0)$  based on the blackbody radiation component found in the bright spiky  $\gamma$ -ray pulse. Right panel: PL radiation spectrum found in the period of  $t_{\rm obs} \in [0, 5]$  s (solid line) and the predicted lower limits of the photospheric emission (magenta and purple solid lines) for different parameters.

**Table 3** Results of Spectral Fits for  $t_{\text{obs}} \in [230, 52000]$  s of GRB 200829A

| GRB         | Interval(s)   | Band    | $\chi_r^2$ | Γ̂               |
|-------------|---------------|---------|------------|------------------|
| GRB 200829A | 230–700       | BAT+XRT | 1.00       | $-2.05 \pm 0.04$ |
|             | 700-2000      | XRT     | 1.11       | $-1.75 \pm 0.01$ |
|             | 5116-7428     | XRT     | 0.94       | $-1.76\pm0.05$   |
|             | 12,119-13,162 | XRT     | 1.09       | $-1.83\pm0.06$   |
|             | 28,067-52,000 | XRT     | 1.19       | $-1.89 \pm 0.06$ |

emission and the late bump with an external-forward shock in the interstellar medium (ISM; see Appendix B for detailed modeling), of which the free parameters are the isotropic kinetic energy  $E_{k,0}$ , the initial Lorentz factor  $\Gamma_0$ , the fraction of shock energy to electron energy  $\epsilon_e$ , the fraction of shock energy to magnetic field energy  $\epsilon_{\scriptscriptstyle B}$ , the interstellar medium density  $n_0$ , the jet opening angle  $\theta_i$ , and  $\delta$ . Here, the energy injection rate of the external-forward shock in the period of  $[t_s, t_e] = [20, 100]$  s is described as  $dE_{\rm inj}/dt_{\rm obs} = E_{\rm k,0}\delta/(t_{\rm e}-t_{\rm s})$  with  $\delta$  being a free parameter in our fitting. In our fitting, a Markov Chain Monte Carlo (MCMC) method based on the emcee Python package (Foreman-Mackey et al. 2013) is adopted to search for the best-fit parameter set. The optimal result is shown in the left panel of Figure 1 with a dark-red line for X-ray data and a blue line for optical data, and the obtained parameters at the  $1\sigma$  confidence level are  $\log_{10} E_{k,0} = 53.65^{+0.07}_{-0.07}$  erg,  $\log_{10} \Gamma_0 = 3.17^{+0.05}_{-0.01}$ ,  $\log_{10} \epsilon_e =$  $-0.31_{-0.01}^{+0.01}, \log_{10} \epsilon_B = -5.15_{-0.19}^{+0.17}, \log_{10} n_0 = 1.27_{-0.18}^{+0.19} cm^{-3},$  $p = 2.001^{+0.002}_{-0.001}, \quad \theta_j = 0.09^{+0.01}_{-0.01}, \quad \log_{10} \delta = 0.81^{+0.04}_{-0.03}.$ corresponding posterior probability density functions for the physical parameters are presented in Figure 5. From the left panel of Figure 1, one can find that the external-forward shock with a refreshed phase can well describe both the very early prompt emission and the late bump in the afterglows for GRB 200829A.

## 4. Summary and Discussions

Observationally, GRB 200829A appears with a weak  $\gamma$ -ray emission in the very early phase, followed by a small  $\gamma$ -ray pulse at around 6 s and a bright spiky  $\gamma$ -ray pulse at around 20 s after the Fermi trigger. After the bright spiky  $\gamma$ -ray pulse, a smooth bump in the X-ray bands appears. We perform a detailed spectral analysis on the very early prompt emission and the bright spiky  $\gamma$ -ray pulse. It reveals that the very early prompt emission can be well fitted by a PL spectral model with index  $\sim$ -1.7. However, the bright spiky  $\gamma$ -ray pulse, especially the time around the pulse peak, exhibits a distinct two-component, i.e., Band function combined with a blackbody

radiation spectrum. This indicates that the origination of the very early prompt emission and the bright spiky  $\gamma$ -ray pulse may be different. The PL spectral index of the very early prompt emission is almost the same as that of the normal decay phase in the X-ray smooth bump, which is suggested to be originated from the external-forward shock. Then, we suggest that the central engine of GRB 200829A may be intermittent and launch several episodes of ejecta separated by a long quiescent interval. The very early phase of the prompt emission originates from the external shock, which is formed during the propagation of the first launched ejecta in the circum-burst medium. The later launched ejecta, of which the internal dissipation is responsible for the two  $\gamma$ -ray pulses, collide with the formed external shock in the period of  $t_{\rm obs} \sim [60, 100]$  s. Then, the energy injection into the external shock is presented in this period and correspondingly a rising phase appears in the period of  $t_{\rm obs} \sim [60, 100]$  s. Based on the above paradigm, we fit the very early prompt emission and the late bump with an external-forward shock in the ISM based on the MCMC method. It is shown that the light curves of the very early prompt emission, X-ray afterglow after 40 s involving the X-ray bump at around 100 s, and the later optical afterglow can be well modeled in the above paradigm.

We also perform a detailed study on the jet producing the bright spiky  $\gamma$ -ray pulse. Based on the blackbody radiation component found in this pulse, the magnetization of the jet at the photosphere is estimated to be  $\sim$ 4 if the initial size of the fireball  $r_0 = 10^9$  cm is adopted. Then, the nonthermal component in the bright spiky  $\gamma$ -rays, i.e., the Band component, seems to be formed during the dissipation of the magnetic energy. This may lead to a high radiation efficiency of the jet. With the energy injection in the period of [20, 100] s, the radiation efficiency of the bright spiky  $\gamma$ -ray pulse is estimated as  $\eta_{\gamma} = E_{\gamma}/(E_{\gamma} + E_{\rm inj}) \sim 52.1\%$ , where  $E_{\rm inj} = dE_{\rm inj}/dt_{\rm obs} \times (t_{\rm e} - t_{\rm s})$  and  $E_{\gamma} \approx 1.41 \times 10^{54}$  erg is the isotropic energy of the bright spiky  $\gamma$ -ray pulse. The obtained high value of radiation efficiency is consistent with the scenario that the nonthermal component in this pulse is formed during the dissipation of the magnetic energy in the jet. Besides, the Lorentz factor of the jet at the photosphere is estimated to be around 500 (400) if  $r_0 = 10^8$  cm ( $r_0 = 10^9$  cm) is adopted. The Lorentz factor of the jet can also be estimated as follows. The distance of the jet dissipation location  $r_{\rm dis}$  relative to the central engine of the burst and the Lorentz factor  $\Gamma_{\mbox{\scriptsize dis}}$  of the dissipation region may be related to the pulse duration  $\Delta t_{\mathrm{pulse}}$  as  $\Delta t_{\rm pulse} = R_{\rm dis}/(2\Gamma_{\rm dis}^2 c) \sim 4 \, {\rm s}$  (FWHM). In addition, the dissipation location should be less than the location of the external shock at the same observer time, i.e.,  $R_{\rm dis} \lesssim R_{\rm es,20~s} \sim 4 \times 10^{16}$ 

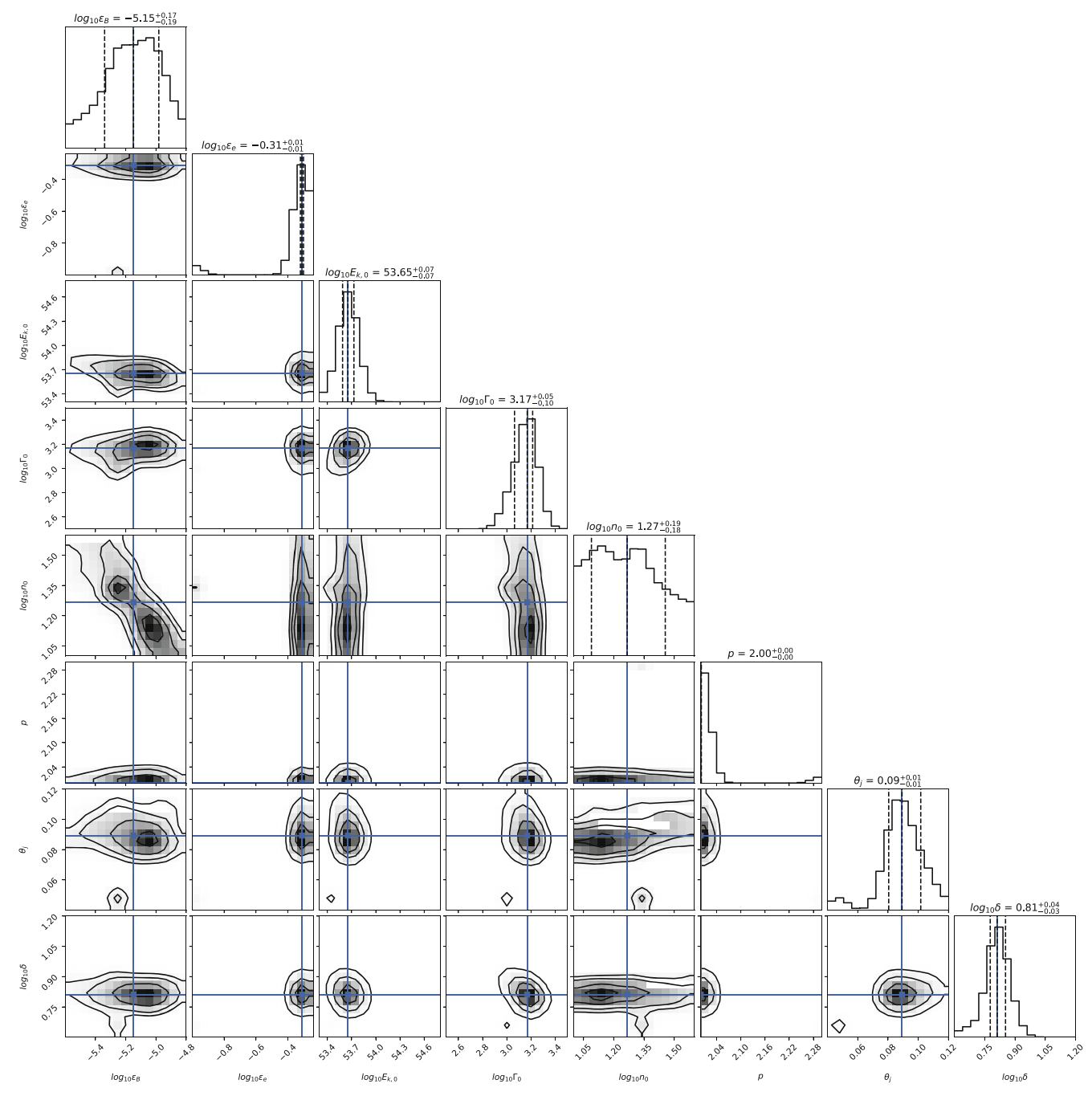


Figure 5. Posterior probability density functions for the physical parameters of the external-forward shock in GRB 200829A from MCMC simulations.

cm, where  $R_{\rm es,20~s}$  is the location of the external shock at the observer time 20 s and obtained based on the initial fireball (without energy injection) and Equations (B1)–(B5). Then, one can have  $\Gamma_{\rm dis}\lesssim 408$ . Interestingly, the Lorentz factor of the jet producing the bright spiky  $\gamma$ -ray pulse can be estimated based on the blackbody radiation component. We find that the Lorentz factor of the jet is consistent with that estimated based on the blackbody radiation component in the bright spiky  $\gamma$ -ray pulse. Please see the left panel of Figure 4, where  $\Gamma_{\rm ph} \sim 400$  is obtained if  $r_0=10^9$  cm is adopted.

The magnetization of the outflow would affect its photospheric emission (e.g., Zhang & Pe'er 2009; Gao & Zhang 2015). Since the emission of the initial fireball, involving the photospheric emission, was missed in the

observation, the magnetization of the initial fireball would be high. In the spirit of Zhang & Pe'er (2009), the outflow with magnetization  $\sigma \gtrsim 125~(\sigma \gtrsim 162)$  is required if  $r_0=10^8~{\rm cm}~(r_0=10^9~{\rm cm})$  is adopted. Here, the luminosity of the initial fireball  $L_{\rm w}$  is estimated as  $L_{\rm w} \sim E_{\rm k,0}/2.5~{\rm s}$ . Corresponding, the related photosphere emission is plotted in the right panel of Figure 5, where the observed PL radiation spectrum in the period of  $t_{\rm obs} \sim [0,\,5]~{\rm s}$  is shown with a black solid.

We thank the anonymous referee of this work for useful comments and suggestions that improved the paper. We acknowledge the use of the Fermi archive's public data. We appreciate Xing Yang for his help in this work. This work is supported by the National Natural Science Foundation of China (grant Nos. 12273005, 12133003, U1938201, and U1938106), the Guangxi Science Foundation (grant Nos. 2018GXNSFFA281010, 2018GXNSFGA281007, and 2018 GXNSFDA281033), and China Manned Spaced Project (CMS-CSST-2021-B11).

# $\begin{array}{c} Appendix\ A\\ Discussion\ about\ the\ Prompt\ Emission\ of\ GRB\ 200829A\ in\\ the\ Period\ of\ [0,\ 5]\ s \end{array}$

In this section, we present a comprehensive discussion about the radiation spectrum in the prompt emission of GRB 200829A in the period of [0, 5] s. We would like to conclude that the intrinsic radiation spectrum in this period may be consistent with a PL spectral model with  $\hat{\Gamma} \sim -1.7$  or a Band function with a break at  $\sim$ 10 MeV and PL index  $\sim$ -1.7 in its low-energy regime ( $E \lesssim 10 \text{ MeV}$ ), rather than a Band function with  $\alpha \sim -1$ ,  $\beta \sim -3$ , and  $E_p \sim 200$  keV. This conclusion is made based on the comprehensive comparison between the spectral fitting results on the observational data and those on the synthetic data of Fermi observation. Here, the synthetic data of Fermi observation is generated based on the python source package threeML13 (Vianello et al. 2015) and the Band function with  $\alpha = -1$ ,  $\beta = -3$ , and  $E_p = 200$  keV is adopted as the intrinsic radiation spectrum to produce synthetic data. In addition, the signal significance of the synthetic data is set as that of the observational data of GRB 200829A in the period of [0, 5] s. The spectral fittings in this section are performed based on the MCMC method to produce posterior predictions for the model parameters<sup>14</sup> and the python source package emcee (Foreman-Mackey et al. 2013) is used for our MCMC sampling. The spectral fitting results are reported in Table 4.

The reasons for our above conclusion are as follows.

1. In the spectral fitting, the values of "Residuals ( $\sigma$ )" (see the bottom part in each panel of Figure 6) provides the most important information to confront the spectral model with the observed data. A good spectral model for the observational data should provide a good distribution of "Residuals ( $\sigma$ )" such as that shown in the bottom part of the upper-right panel in Figure 6. In Figure 6, the upper-left and upper-right panels show the spectral fitting results on the synthetic data with a PL model and a Band function, respectively. Since the intrinsic radiation spectrum of the synthetic data is a Band function with  $E_p = 200$  keV, the spectral fitting on the synthetic data with a Band function should provide an optimal fitting. Actually, the values of the corresponding "Residuals  $(\sigma)$ " are indeed well distributed around zero. In the spectral fitting on the synthetic data with a PL model, however, the values of "Residuals ( $\sigma$ )" appear as positive around  $E_p$  and negative below/above  $\sim E_p$ . It reveals that even though the Band function with  $\alpha = -1$ ,  $\beta = -3$ , and  $E_p = 200$  keV can be described as a PL model with  $\hat{\Gamma} \sim -1.65$  (see the second line of Table 4), the observational data would exceed the PL model around  $E_{\rm p}$  and fail to reach the PL model below/above  $\sim\!\!E_{\rm p}$ . This behavior is consistent with the theoretical expectation. In

the bottom-left and bottom-right panels of Figure 6, we show the spectral fitting results on the observational data of GRB 200829A in the period of [0, 5] s with a PL spectral model and a Band function, respectively. The spectral fitting results are also reported in the fourth and fifth lines of Table 4. One can find that "Residuals ( $\sigma$ )" in these two panels are well distributed around zero, which is very similar to that in the upper-right panel. It implies that the intrinsic radiation spectrum of this period should be consistent with a PL spectral model with  $\hat{\Gamma} \sim -1.7$  or a Band function with a break at ∼10 MeV and PL index  $\sim$ -1.7 in its low-energy regime ( $E \lesssim 10$  MeV), rather than a Band function with  $\alpha \sim -1$ ,  $\beta \sim -3$ , and  $E_p \sim 200$ keV. This is because if the intrinsic radiation spectrum of the observational data is a Band function with  $\alpha \sim -1$ .  $\beta \sim -3$ , and  $E_p = 200$  keV, the values of "Residuals ( $\sigma$ )" would be positive  $\sim 200 \text{ keV}$  and negative below/above  $\sim$ 200 keV on average. However, this behavior could not be evidently found in the bottom-left panel of Figure 6.

2. If the intrinsic radiation spectrum in this period is the Band function with  $E_0 \sim 200$  keV, the spectral fitting results on the low-energy regime, e.g., the energy band of Swift-BAT (15-150 keV), with a PL spectral model would be very different from that on the energy band of Fermi-GBM instrument (8 keV-40 MeV). Then, we perform the spectral fittings on the data in the 15-150 keV energy band. The posterior probability density functions for the physical parameters of the spectral model are shown in Figure 7, where the upper and bottom panels are the spectral fitting results on the synthetic data and the observational data in the 15-150 keV energy band, respectively. A PL spectral model and Band function are adopted in the spectral fittings for the left and right panels, respectively. It is shown that the spectral fittings on the synthetic data with a PL spectral model for different energy regimes are indeed presented with very different values of the PL index  $\hat{\Gamma}$ , i.e.,  $\hat{\Gamma} = -1.65^{+0.04}_{-0.04}$ for the 8 keV-40 MeV energy band and  $\hat{\Gamma} = -1.44^{+0.10}_{-0.10}$ for the 15-150 keV energy band. Interestingly, the spectral fittings on the synthetic data with a Band function almost report the same values of  $\alpha$ ,  $\beta$ , and  $E_0$ for the 15–150 keV energy band and the 8 keV–40 MeV energy band. According to the fitting results reported in Table 4, one can find that the spectral fittings on the observational data in the 15-150 keV energy band and those in the 8 keV-40 MeV energy band almost presented the same fitting results. Please compare the eighth line with the fourth line or the ninth line with the fifth line in Table 4. It implies that the radiation spectrum in this period should be consistent with a PL spectral model with  $\hat{\Gamma} \sim -1.7$  or a Band function with a break at  $\sim$ 10 MeV and PL index  $\sim$ -1.7 in its low-energy regime  $(E \lesssim 10 \text{ MeV})$ , rather than a Band function with  $\alpha \sim -1$ ,  $\beta \sim -3$ , and  $E_p \sim 200$  keV.

In summary, by comparing the spectral fitting results on the observational data to those on the synthetic data, we can conclude that the intrinsic radiation spectrum in this period should be consistent with a PL spectral model with  $\hat{\Gamma} \sim -1.7$  or a Band function with a break at  $\sim 10$  MeV and PL index  $\sim -1.7$  in its low-energy regime ( $E \lesssim 10$  MeV).

https://github.com/threeML/threeML

<sup>&</sup>lt;sup>14</sup> This method is different from that used in the main text of the present paper. In the main text, the spectral model parameters are obtained based on the package Xspec by maximizing the likelihood. However, one can find that the model parameters are consistent with each other in these two fitting methods.

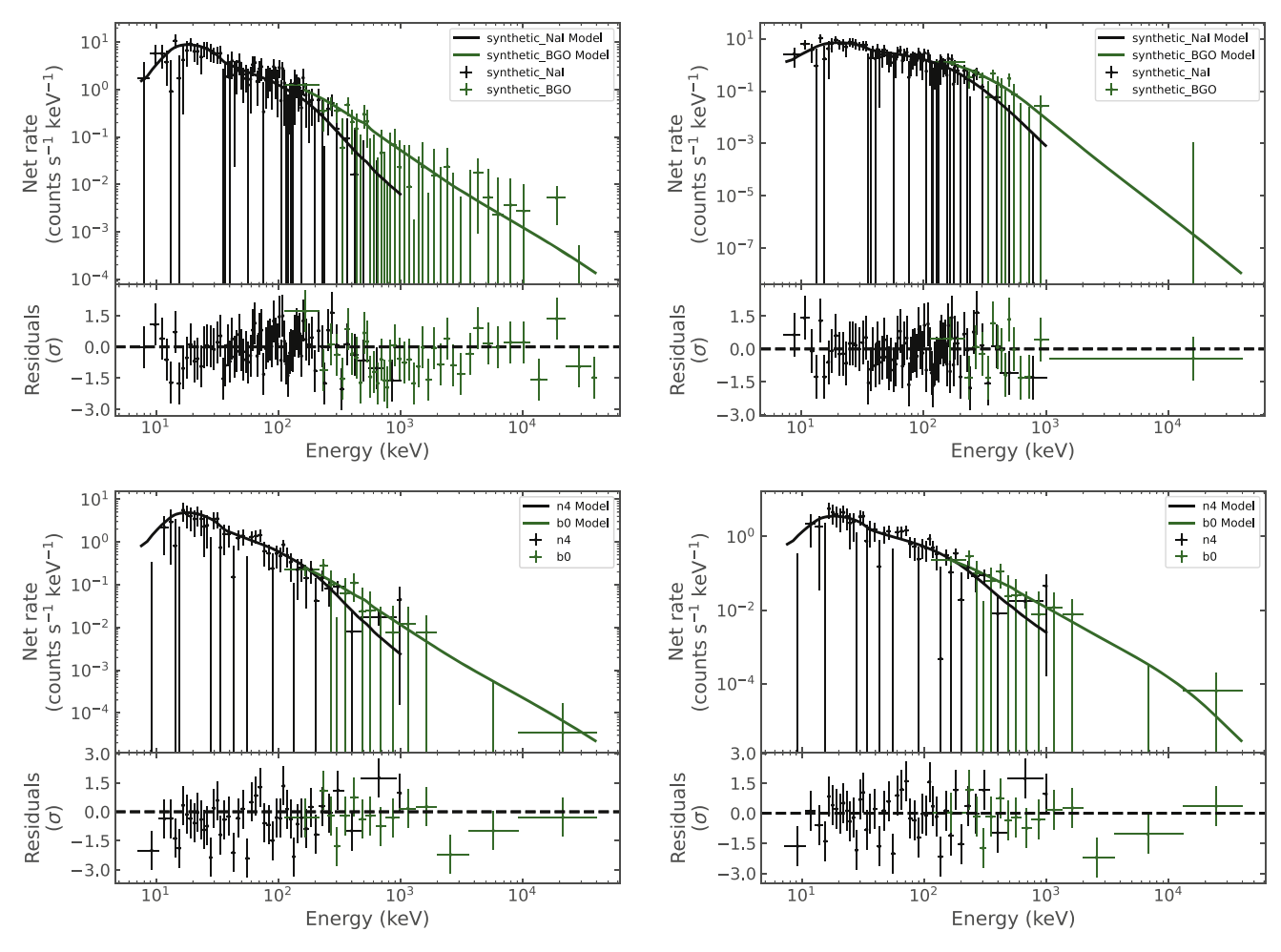


Figure 6. Fitting results of the synthetic data (upper panels) and the observational data (bottom panels) in the 8 keV-40 MeV energy band, where a PL spectral model and Band function are adopted in the left and right panels, respectively.

 Table 4

 Spectral Fitting Results of Simulation and Observation of [0, 5] s in GRB 200829A

| Model | $\alpha \text{ (or } \hat{\Gamma})$ | β                       | $E_0(\text{keV})$                  | $N_0$                                   | Data Sources                      |
|-------|-------------------------------------|-------------------------|------------------------------------|---|-----------------------------------|
| PL    | $-1.65^{+0.04}_{-0.04}$             |                         |                                    | 31.52+6.14                              | synthetic data (8 keV–40 MeV)     |
| Band  | $-1.16^{+0.14}_{-0.11}$             | $-3.71^{+0.88}_{-0.83}$ | $276.67^{+91.20}_{-71.06}$         | $0.03^{+0.01}_{-0.00}$                  | synthetic data (8 keV-40 MeV)     |
| PL    | $-1.73^{+0.08}_{-0.09}$             |                         |                                    | $15.65^{+11.32}_{-7.15}$                | observational data (8 keV-40 MeV) |
| Band  | $-1.61^{+0.10}_{-0.11}$             | $-2.94^{+0.85}_{-1.21}$ | $11021.76^{+13229.91}_{-5533.27}$  | $0.00\pm0.00$                           | observational data (8 keV-40 MeV) |
| PL    | $-1.44^{+0.10}_{-0.10}$             |                         |                                    | 13.49 <sup>+7.00</sup> <sub>-4.68</sub> | synthetic data (15–150 keV)       |
| Band  | $-1.09^{+0.17}_{-0.15}$             | $-3.25^{+1.19}_{-1.26}$ | $268.28^{+141.98}_{-110.57}$       | $0.03^{+0.01}_{-0.00}$                  | synthetic data (15-150 keV)       |
| PL    | $-1.71^{+0.14}_{-0.15}$             |                         |                                    | $19.06^{+17.86}_{-9.79}$                | observational data (15-150 keV)   |
| Band  | $-1.62^{+0.15}_{-0.17}$             | $-3.47^{+1.14}_{-0.98}$ | $18813.06^{+34951.87}_{-11705.06}$ | $0.00\pm0.00$                           | observational data (15-150 keV)   |

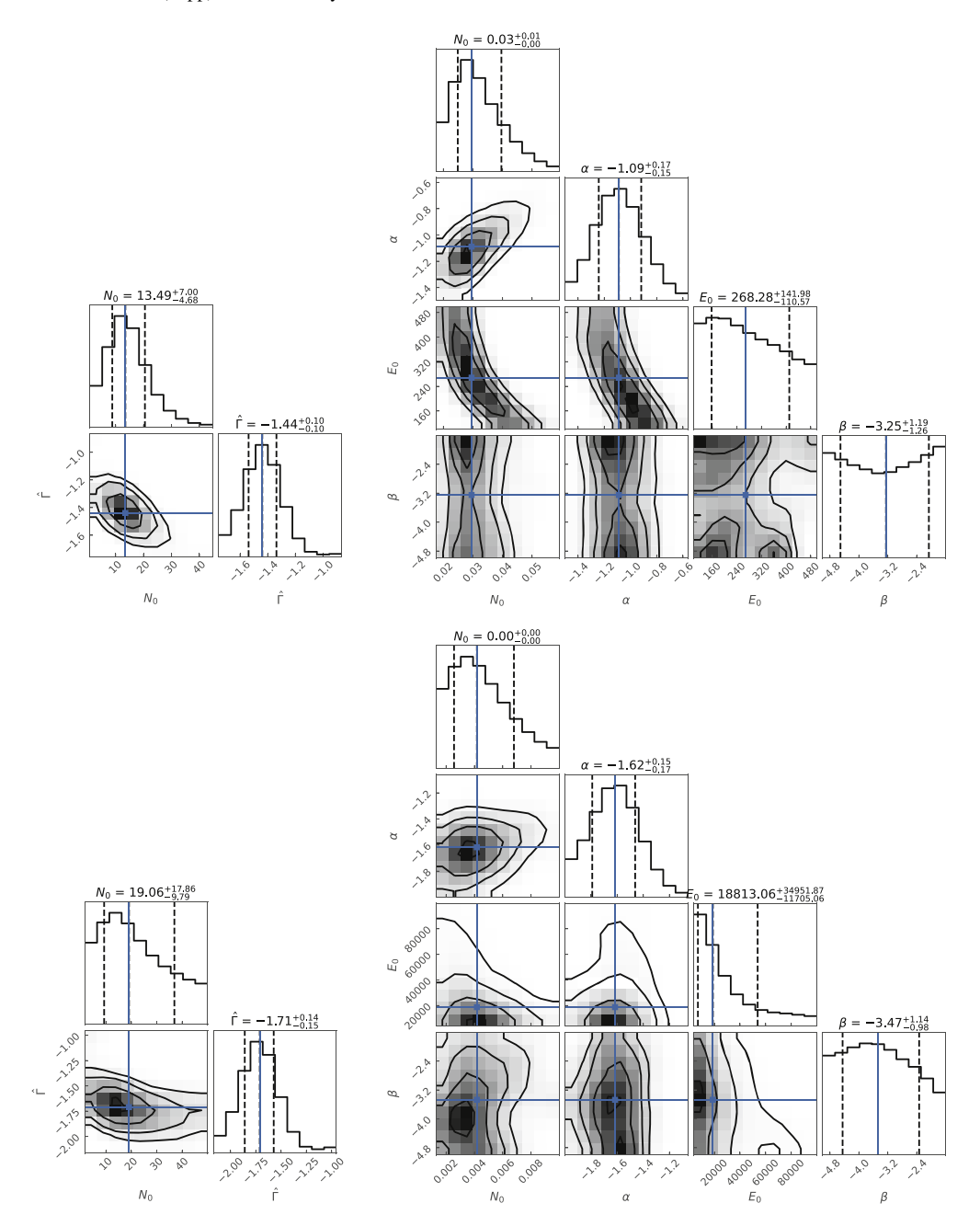


Figure 7. Posterior probability density functions for the physical parameters of the spectral fitting on the synthetic data (upper panels) and the observational data (bottom panels) in the 15–150 keV energy band, where a PL spectral model and Band function are adopted in the left and right panels, respectively.

## Appendix B Model

In this section, the dynamics and the emission of the external-forward shock are presented as follows. The dynamics of the external-forward shock can be described with the following equations (e.g., Sari et al. 1998; Huang et al. 1999):

$$\frac{d\Gamma}{dt_{\rm obs}} = \frac{1}{M'} \left[ \frac{1}{c^2} \frac{dE_{\rm inj}}{dt_{\rm obs}} - (\Gamma^2 - 1) \frac{dm}{dt_{\rm obs}} \right], \tag{B1}$$

$$\frac{dm}{dt_{\rm obs}} = 4\pi \rho R^2 \frac{dR}{dt_{\rm obs}},\tag{B2}$$

$$\frac{dU'}{dt_{\text{obs}}} = (1 - \epsilon)(\Gamma - 1)c^2 \frac{dm}{dt_{\text{obs}}},$$
 (B3)

$$\frac{dR}{dt_{\text{obs}}} = \frac{c\beta}{1-\beta}(1+z),\tag{B4}$$

$$\beta = \sqrt{1 - 1/\Gamma^2},\tag{B5}$$

where  $\Gamma$ ,  $dE_{\rm inj}/dt_{\rm obs}$ , R,  $\epsilon$ , and  $c\beta$  are the Lorentz factor, the energy injection rate (with respect to the observer time  $t_{\rm obs}$ ), location, the radiation efficiency, and the velocity of the external-forward shock, and  $M' = M'_{\rm ej} + m + U'/c^2$  is the total mass, including the initial mass  $M'_{\rm ej} = E_{\rm k,0}/[(\Gamma_0 - 1)c^2]$  of the ejecta, the sweep-up mass m from the circum-burst medium, and the internal energy U' of the shocked material from the external shock. Here,  $E_{\rm k,0}$  is the initial isotropic kinetic energy of the fireball,  $\Gamma_0 = \Gamma(t_{\rm obs} = 0)$  is the initial bulk Lorentz factor of the fireball, c is the velocity of light, c is the redshift of the burst, and

 $\rho$  is the density of the circum-burst environment. Two cases of a circum-burst medium, i.e., ISM and wind, are generally studied. Correspondingly, we take (e.g., Chevalier & Li 2000)

$$\rho = \begin{cases} 5 \times 10^{11} A_* R^{-2} \text{ g} \cdot \text{cm}^{-1}, & \text{wind,} \\ n_0 m_p \text{ cm}^{-3}, & \text{ISM,} \end{cases}$$
(B6)

with  $m_p$  being the proton mass,  $A_*$  is a dimensionless constant. For simplicity, the energy injection into the external shock due to the late activity of the central engine is assumed with a constant energy injection rate over the period of  $t_{\rm obs} \in [t_{\rm s}, t_{\rm e}]$ , where  $t_{\rm s}$  and  $t_{\rm e}$  are the beginning and the end of the energy injection, respectively. By describing  $E_{\rm inj}$  as  $E_{\rm inj} = E_{\rm k,0} \delta$ , one thus can have  $dE_{\rm inj}/dt_{\rm obs} = E_{\rm k,0} \delta/(t_{\rm e} - t_{\rm s})$ .

The main radiation mechanism of the external-forward shock in GRBs is the synchrotron radiation of the sweep-up electrons (Sari et al. 1998; Sari & Piran 1999).  $\epsilon_{\rm e}$  and  $\epsilon_{\rm B}$  are introduced to represent the fractions of the shock energy used to accelerate electrons and contribute to the magnetic energy, respectively. Then, the magnetic field behind the shock is  $B'=(32\pi\epsilon_B\rho/m_{\rm p})^{1/2}\Gamma c$ . The sweep-up electrons are accelerated to a PL distribution of Lorentz factor  $\gamma_e$ , i.e.,  $Q\propto\gamma'_e^{-p}$  for  $\gamma'_{e,{\rm min}}\leqslant\gamma_e\leqslant\gamma'_{e,{\rm max}}$ , where p(>2) is the PL index,  $\gamma_{e,{\rm min}}=\epsilon_e(p-2)m_{\rm p}\Gamma/[(p-1)m_{\rm e}]$  (Sari et al. 1998), and  $\gamma_{e,{\rm max}}=\sqrt{9m_{\rm e}^2c^4/(8B'q_e^3)}$  with  $q_{\rm e}$  being the electron charge (e.g., Kumar et al. 2012). Then, one can have  $\epsilon=\epsilon_{\rm rad}\epsilon_e$  with  $\epsilon_{\rm rad}=\min\{1,(\gamma_{e,{\rm min}}/\gamma_{e,c})^{(p-2)}\}$  (Fan & Piran 2006), where  $\gamma_{e,c}=6\pi m_e c(1+z)/(\sigma_{\rm T}\Gamma B'^2 t_{\rm obs})$  is the efficient cooling Lorentz factor of electrons.

Equations (B1)–(B5) describe the evolution of hydrodynamic blastwave approximately. A more rigorous treatment can be found in Nava et al. (2013) and Zhang (2018; see Equation (8.66) in this book). For our studied burst, the blastwave is affected by the energy injection, and thus its evolution could not be simply estimated with hydrodynamic equations in Nava et al. (2013) and Zhang (2018). More complicated equations are required. For the phase without energy injection, we also present the light curve of afterglows based on the hydrodynamic equations in Nava et al. (2013) and Zhang (2018). It is found that the obtained light curves of afterglows are almost the same as those obtained with Equations (B1)–(B5).

## ORCID iDs

Jing Li https://orcid.org/0000-0002-6019-7381

Da-Bin Lin https://orcid.org/0000-0003-1474-293X

Rui-Jing Lu https://orcid.org/0000-0003-2467-3608

Xiang-Gao Wang https://orcid.org/0000-0001-8411-8011

En-Wei Liang https://orcid.org/0000-0002-7044-733X

## References

Band, D., Matteson, J., Ford, L., et al. 1993, ApJ, 413, 281 Beloborodov, A. M. 2010, MNRAS, 407, 1033

```
Burgess, J. M., Bégué, D., Ryde, F., et al. 2016, ApJ, 822, 63
Burnham, K. P., & Anderson, D. R. 2004, Sociol. Method. Res., 33, 261
Chevalier, R. A., & Li, Z.-Y. 2000, ApJ, 536, 195
Colgate, S. A. 1974, ApJ, 187, 333
De Pasquale, M. 2020, GCN, 28404, 1
Deng, L.-T., Lin, D.-B., Zhou, L., et al. 2022, ApJL, 934, L22
Eichler, D., Livio, M., Piran, T., & Schramm, D. N. 1989, Natur, 340, 126
Fan, Y., & Piran, T. 2006, MNRAS, 370, L24
Foreman-Mackey, D., Hogg, D. W., Lang, D., & Goodman, J. 2013, PASP,
  125, 306
Gao, H., & Zhang, B. 2015, ApJ, 801, 103
Ghirlanda, G., Pescalli, A., & Ghisellini, G. 2013, MNRAS, 432, 3237
Giannios, D. 2008, A&A, 480, 305
Gropp, J. D., Kennea, J. A., Beardmore, A. P., et al. 2020, GCN, 28317, 1
Guiriec, S., Mochkovitch, R., Piran, T., et al. 2015, ApJ, 814, 10
Guiriec, S., Daigne, F., Hascoët, R., et al. 2013, ApJ, 770, 32
Hentunen, V.-P., & Nissinen, M. 2020, GCN, 28318, 1
Huang, L.-Y., Wang, X.-G., Zheng, W., et al. 2018, ApJ, 859, 163
Huang, Y. F., Dai, Z. G., & Lu, T. 1999, MNRAS, 309, 513
Izzo, L. 2020, GCN, 28331, 1
Kuin, N. P. M., Siegel, M. H. & Swift/UVOT Team 2020, GCN, 28311, 1
Kumar, P., Hernández, R. A., Bošnjak, Ž, & Barniol Duran, R. 2012, MNRAS,
  427, L40
Kumar, P., & Zhang, B. 2015, PhR, 561, 1
Lesage, S., Meegan, C. & Fermi GBM Team 2020, GCN, 28326, 1
Lin, D.-B., Huang, B.-Q., Liu, T., et al. 2018, ApJ, 852, 136
Lipunov, V., Kornilov, V., Gorbovskoy, E., et al. 2020a, GCN, 28315, 1
Lipunov, V., Kornilov, V., Gorbovskoy, E., et al. 2020b, GCN, 28309, 1
MacFadyen, A. I., & Woosley, S. E. 1999, ApJ, 524, 262
Meszaros, P., & Rees, M. J. 1993, ApJ, 405, 278
Mészáros, P., & Rees, M. J. 1997, ApJ, 476, 232
Moskvitin, A. S., Aitov, V. N. & GRB follow-up Team 2020a, GCN,
   28328, 1
Moskvitin, A. S., Aitov, V. N. & GRB follow-up Team 2020b, GCN, 28322, 1
Narayan, R., Paczynski, B., & Piran, T. 1992, ApJL, 395, L83
Nava, L., Sironi, L., Ghisellini, G., Celotti, A., & Ghirlanda, G. 2013,
  MNRAS, 433, 2107
Nousek, J. A., Kouveliotou, C., Grupe, D., et al. 2006, ApJ, 642, 389
Oates, S. R., Kuin, N. P. M., De Pasquale, M., et al. 2020, GCN, 28338, 1
Paczynski, B. 1986, ApJL, 308, L43
Palmer, D. M., Barthelmy, S. D., Cummings, J. R., et al. 2020, GCN, 28325, 1
Pankov, N., Novichonok, A., Zhornichenko, A., et al. 2020, GCN, 28329, 1
Piran, T. 2004, RvMP, 76, 1143
Poolakkil, S., Preece, R., Fletcher, C., et al. 2021, ApJ, 913, 60
Pozanenko, A., Reva, I., Serebryanskiy, A., et al. 2020a, GCN, 28308, 1
Pozanenko, A., Pankov, N., Belkin, S., et al. 2020b, GCN, 28359, 1
Rees, M. J., & Meszaros, P. 1992, MNRAS, 258, 41
Rees, M. J., & Meszaros, P. 1994, ApJL, 430, L93
Sari, R., & Piran, T. 1999, ApJL, 517, L109
Sari, R., Piran, T., & Narayan, R. 1998, ApJL, 497, L17
Schwarz, G. 1978, AnSta, 6, 461
Siegel, M. H., Gropp, J. D., Kennea, J. A., et al. 2020, GCN, 28307, 1
Vianello, G., Lauer, R. J., Younk, P., et al. 2015, arXiv:1507.08343
Volnova, A., Naroenkov, S., Pozanenko, A., et al. 2020, GCN, 28333, 1
Vurm, I., Beloborodov, A. M., & Poutanen, J. 2011, ApJ, 738, 77
Woosley, S. E. 1993, ApJ, 405, 273
Woosley, S. E., & Bloom, J. S. 2006, ARA&A, 44, 507
Zhang, B. 2018, The Physics of Gamma-Ray Bursts (Cambridge: Cambridge
  Univ. Press)
Zhang, B., Fan, Y. Z., Dyks, J., et al. 2006, ApJ, 642, 354
Zhang, B., & Mészáros, P. 2004, IJMPA, 19, 2385
Zhang, B., & Pe'er, A. 2009, ApJL, 700, L65
Zhang, B., & Yan, H. 2011, ApJ, 726, 90
Zhu, Z. P. Y., Fu, S., Liu, X., et al. 2020a, GCN, 28330, 1
Zhu, Z. P. Y., Fu, S., Liu, X., et al. 2020b, GCN, 28324, 1
```